Scientific Reports

https://doi.org/10.1038/s41598-026-38782-3

Article in Press

Assessment of cognitive load through photoplethysmography and bioimpedance responses during mental arithmetic tasks

Received: 28 September 2025

Accepted: 31 January 2026

Published online: 05 February 2026

Cite this article as: Huynh D.N., Tran T.N., Tran K.T. *et al.* Assessment of cognitive load through photoplethysmography and bioimpedance responses during mental arithmetic tasks. *Sci Rep* (2026). https://doi.org/10.1038/s41598-026-38782-3

Dang Nguyen Huynh, Thao Nguyen Tran, Khang Thanh Tran, Nguyen Khoa Le, Cao Dang Le, Huu-Xuan Mai, Quang-Linh Huynh & Trung-Hau Nguyen

Assessment of cognitive load through photoplethysmography and bioimpedance responses during mental arithmetic tasks

Dang Nguyen Huynh[1,2], Thao Nguyen Tran[1,2], Khang Thanh Tran[1,2], Nguyen Khoa Le[1,2], Cao Dang Le[1,2], Huu-Xuan Mai[1,2], Quang-Linh Huynh[1,2], and Trung-Hau Nguyen[1,2,*]

[1]Department of Biomedical Engineering, Faculty of Applied Science, Ho Chi Minh City University of Technology (HCMUT), 268 Ly Thuong Kiet Street, Dien Hong Ward, Ho Chi Minh City 700000, Vietnam
[2]Vietnam National University Ho Chi Minh City, Linh Xuan Ward, Ho Chi Minh City 700000, Vietnam
[*]haunguyen85@hcmut.edu.vn

ABSTRACT

Accurate assessment of cognitive load is vital in cognitive research and human–machine interaction. This study investigates a multimodal approach for classifying graded cognitive load levels using cardiovascular signals derived from photoplethysmography (PPG) and impedance plethysmography (IPG). Data were collected from 15 healthy adults performing mental arithmetic tasks of increasing difficulty (Rest, Level 1, Level 2, and Level 3). Carotid PPG was used as a global indicator of cerebral perfusion, while frontal IPG captured localized changes in regional blood volume. Machine learning algorithms, including Decision Trees, Random Forest, and XGBoost, were applied to discriminate between workload levels. Among these models, Random Forest achieved the highest performance, reaching 96% accuracy in subject-dependent classification. Subject-independent accuracy was lower (66%), reflecting substantial inter-subject variability. IPG-derived features were among the most influential contributors to workload discrimination, highlighting the role of localized neurovascular responses to cognitive demand. These findings support the potential of PPG–IPG fusion as a noninvasive and physiologically grounded technique for continuous monitoring of cognitive workload.

Introduction

Accurately assessing cognitive load has become increasingly important in modern high-stakes environments such as aviation, healthcare, education, and complex industrial operations[1–4]. Effective detection and management of cognitive load can enhance human performance, reduce errors, and improve overall safety and well-being. Reliable identification of cognitive overload and fatigue enables timely interventions that support optimal task execution and protect operator health[4–9].

Traditional approaches to cognitive load assessment have largely relied on single-modality measurements, particularly electroencephalography (EEG), due to its direct link to neural activity[10–14]. For example, Dimitrakopoulos et al.[15] reported 87% accuracy in classifying two levels of workload using multiband EEG cortical connectivity. Although EEG provides rich information about cognitive states, it faces practical limitations such as complex sensor setup, susceptibility to motion and environmental artifacts, and user discomfort associated with through-hair electrode placement. These limitations have motivated the exploration of alternative or complementary methods that are more practical for real-world and wearable applications.

Cardiovascular-based measurements have emerged as strong candidates. Qu et al. (2021)[16] achieved a mean precision of 90.88% using electrocardiography (ECG)-derived features in a two-class workload task, while Fawwaz et al. (2024)[17] reported 81.97% accuracy using a combination of heart rate variability (HRV) and electrodermal activity (EDA), also in a two-class setting. Despite these advances, single-modality systems remain limited, either in performance or in their ability to handle multi-level cognitive load. This reinforces the need for multimodal approaches that integrate complementary physiological signals to enhance accuracy, robustness, and generalizability.

Recent studies have highlighted the close interplay between the brain and the cardiovascular system during cognitive demands[18–20]. This brain–heart interaction is regulated by the autonomic nervous system (ANS), where increased cognitive load alters the balance between sympathetic and parasympathetic activity. These shifts influence heart rate, heart rate variability, vascular tone, and blood pressure, making cardiovascular responses reliable indirect markers of cognitive load[21–24]. Accordingly, we hypothesized that higher cognitive demand would elevate cerebral perfusion, making carotid-based measurements particularly informative.

Pulse Transit Time (PTT) also provides valuable insight into cognitive load due to its well-established relationship with

blood pressure. Increases in blood pressure shorten PTT, while decreases lengthen it[25]. During periods of high cognitive load, sympathetic activation increases the release of catecholamines, enhances cardiac contractility, and causes peripheral vasoconstriction, which reduces arterial compliance[26]. These physiological changes elevate arterial blood pressure above baseline and accelerate pulse wave propagation, thereby shortening PTT[25]. In this study, carotid photoplethysmography (PPG) was used to capture global blood supply to the brain, while forehead impedance plethysmography (IPG) captured localized perfusion changes during cognitive stimulation. The fusion feature, PTT, was derived from the timing difference between the two measurement sites, enabling integration of global and regional hemodynamic information relevant to cognitive load.

Building on this physiological foundation, the present study investigates a multimodal framework for multi-class cognitive load classification using PPG and IPG signals. PPG captures peripheral blood volume changes, while IPG measures tissue impedance variations associated with pulsatile cerebral blood flow. Both techniques are low-cost, comfortable, and well suited for wearable applications, making them practical alternatives or complementary tools to EEG. This study evaluates the contribution and reliability of PPG–IPG fusion for classifying cognitive load during mental arithmetic tasks and examines how task difficulty affects cardiovascular dynamics. The integration of artificial intelligence further enhances the feasibility of such systems, as machine learning algorithms can efficiently extract and combine features from multimodal cardiovascular signals to enable accurate, real-time cognitive load monitoring[27–29].

Methodology

The proposed wearable device

PPG signal acquisition

PPG signal was measured using a MAX30102 optical sensor (Analog Devices, Massachusetts, USA) positioned on the neck over the common carotid artery (Fig. 1(a)). This location provides a clear optical pathway for detecting arterial pulse–induced changes in light reflectance and is preferred over ECG electrode sites, as PPG measures vascular light absorption rather than cardiac electrical activity. The MAX30102 integrates red (660 nm) and infrared (880–940 nm) light-emitting diodes (LEDs) for optical sensing, with the red wavelength exhibiting strong absorption by oxygenated hemoglobin and thus providing high sensitivity for PPG measurements.

During operation, the sensor illuminates the tissue and records the reflected intensity, enabling real-time monitoring of blood volume fluctuations over the cardiac cycle. PPG exploits the fact that tissue absorption varies with pulsatile changes in arterial blood volume. According to the modified Beer–Lambert law, detected intensity decays exponentially with absorption; therefore, in reflectance PPG the photodetector signal varies exponentially with the pulsatile blood volume[30–33].

IPG signal acquisition

IPG acquisition was performed using a four-electrode (tetrapolar) configuration to minimize the influence of electrode–skin interface impedance and to improve measurement accuracy[34,35]. For cerebral monitoring, electrodes were placed on the forehead over the frontal cortex (Fig. 1(a)). The outer electrode pair delivered the excitation current, while the inner pair measured the resulting voltage drop across the targeted tissue segment, producing a pulsatile impedance waveform driven by cardiac-induced changes in blood volume.

The AD5933 (Texas Instruments, Dallas, USA) served as the bioimpedance module. It generates a sinusoidal excitation voltage and measures the corresponding voltage drop in terms of magnitude and phase. The AD5933 is an integrated impedance measurement circuit that contains a frequency generator, a 12-bit analog-to-digital converter (ADC) operating at 1 MSPS, and a digital signal processing unit. It operates with a supply voltage between 2.7 V and 5.5 V and measures impedance within a range of 1 kΩ to 10 MΩ, with extended capability down to approximately 100 Ω when additional circuitry is used. The device supports excitation frequencies up to 100 kHz with 27-bit tuning resolution[36].

In this study, a fixed excitation frequency of 50 kHz was selected. This frequency is commonly used in soft-tissue bioimpedance and arterial assessments and eliminates the need for frequency sweeping, which simplifies hardware design and enhances portability[37–40]. At 50 kHz, the measurement primarily reflects extracellular ionic conduction, including blood, with partial contributions from cell-membrane capacitance[37,38]. Under these conditions, the impedance behaves mainly as a resistive component, and the instantaneous impedance is inversely proportional to the conductive cross-sectional area, which increases with blood volume[37,41]:

$$Z(t) = \frac{\rho L}{A(t)}$$

, where:

- $Z(t)$ is the instantaneous impedance at time t (in Ohms, Ω).

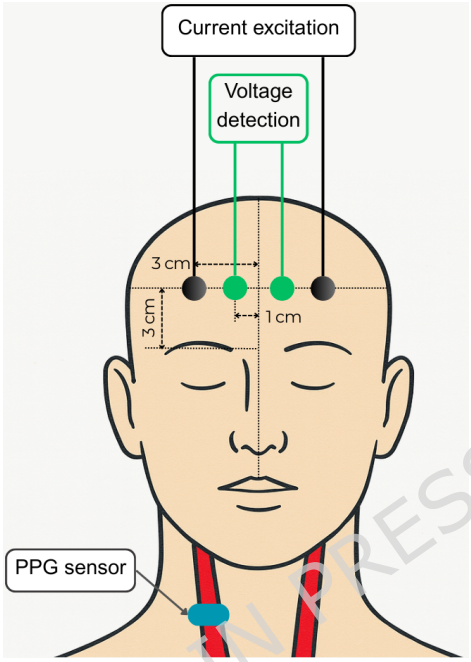

(a)

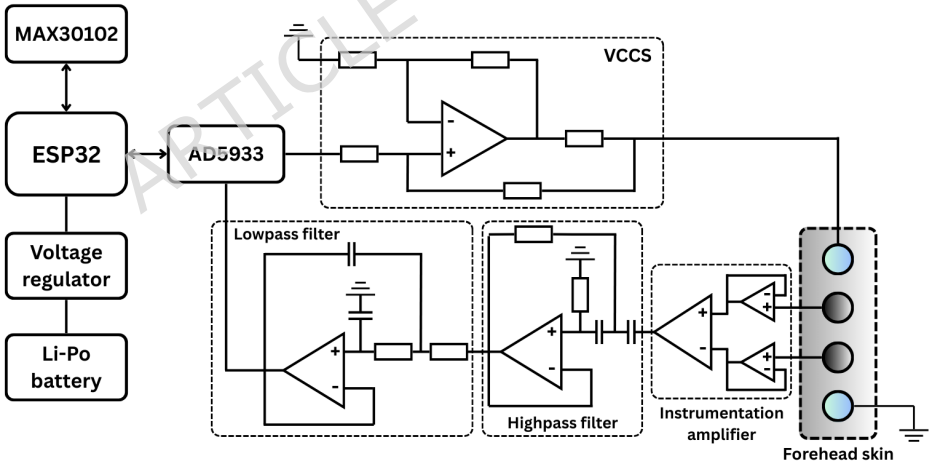

(b)

Figure 1. (a) Body locations for PPG and IPG sensor placement, and (b) functional block diagram of the complete proposed system.

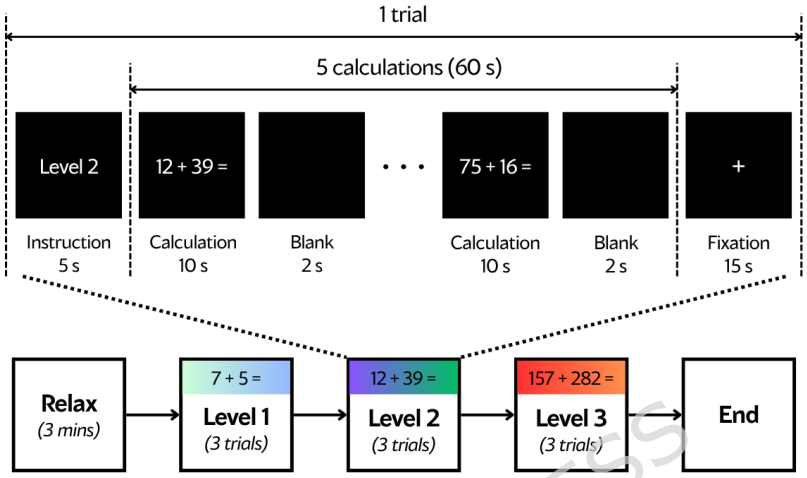

(a)

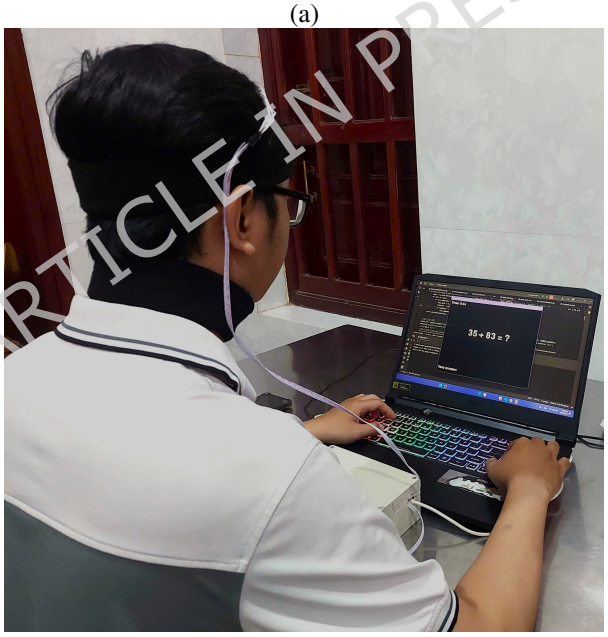

(b)

Figure 2. (a) Experimental paradigm and (b) photograph of the experimental setup.

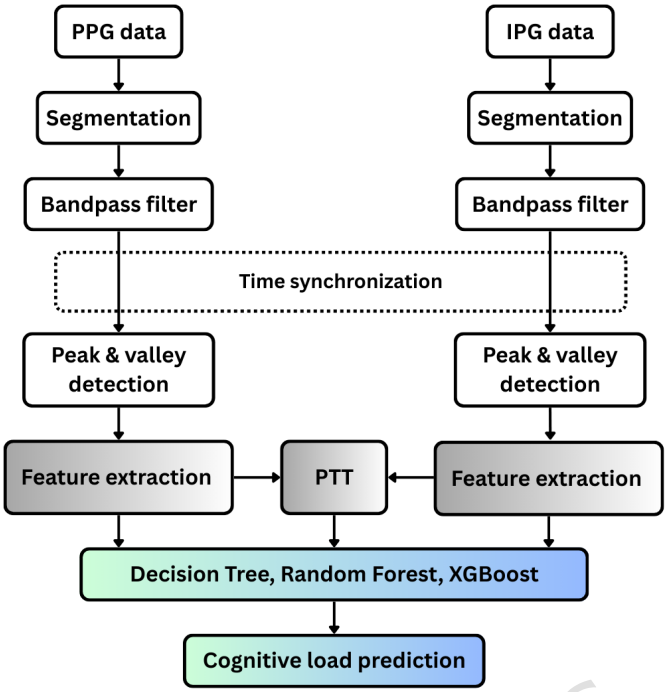

Figure 3. Feature extraction workflow from PPG, IPG, and fused PPG–IPG signals.

- L is the distance between the sensing electrodes (in meters, m).
- ρ is the resistivity of blood (in Ω·m).
- $A(t)$ is the time-varying cross-sectional area of the vessel (in m^2).

During systole, arterial expansion increases the cross-sectional area $A(t)$, thereby reducing impedance. Conversely, during diastole, arterial contraction decreases $A(t)$ and raises impedance. These cyclical changes form the basis of IPG, capturing pulsatile blood flow dynamics. These cyclic changes constitute the IPG signal, which, although small (milliohms to ohms), can be resolved by the AD5933 thanks to its sensitivity and phase measurement capability.

In the proposed design, the AD5933 is integrated with a voltage-controlled current source (VCCS) to deliver a constant 1 mA sinusoidal current for bioimpedance measurement, which complies with established biomedical safety standards[42–44]. As illustrated in Fig. 1(b), an improved Howland current pump is adopted to generate the stable 1 mA current source[45]. For IPG signal acquisition, wet Ag/AgCl ECG electrodes are employed due to their low contact impedance and biocompatibility. A custom signal-conditioning circuit is implemented to ensure high signal fidelity. The low-amplitude voltage acquired from the sensing electrodes is initially amplified using an INA128 instrumentation amplifier (Texas Instruments, Dallas, USA) with a common-mode rejection ratio (CMRR) of 110 dB. The amplified signal is then processed by a second-order active high-pass filter with a cutoff frequency of 0.2 Hz to suppress baseline drift, followed by a fourth-order active low-pass filter with a cutoff frequency of 106 kHz to attenuate high-frequency noise and isolate cardiac-related impedance fluctuations modulated on the 50 kHz excitation carrier.

An ESP32 microcontroller manages communication and control for both sensing modules, the AD5933 impedance converter and the MAX30102, through the I^2C interface, enabling synchronized and reliable multimodal data acquisition (Fig. 1(b)). The combined acquisition of PPG and IPG facilitates multimodal cardiovascular monitoring of both cerebral and peripheral hemodynamics within a compact wearable platform.

Experimental protocol

A total of 15 healthy volunteers participated in this study, comprising 6 females and 9 males, aged between 20 and 35 years. The study protocol was approved by the Ethics Committee of Ho Chi Minh City University of Technology, Vietnam National University, and all procedures were conducted in accordance with the Declaration of Helsinki. Written informed consent was obtained from all participants prior to enrollment. The experimental protocol is illustrated in Fig. 2(a). To elicit different levels of cognitive load, participants performed a series of arithmetic tasks with systematically increasing difficulty. The experimental protocol comprised three difficulty levels in addition to a resting condition.

Each trial began with a 5-second instruction screen, followed by five calculations of mental arithmetic. The difficulty of the problems increased across sessions to progressively elevate cognitive load[46–49]. After completing the set of calculations, participants entered a 15-second relaxation phase in which a fixation cross was displayed on the screen, serving as the resting baseline condition. Each participant completed three such trials during the session.

The task difficulty levels were defined according to the number of digits involved in each addition problem. Level 1 consisted of adding two single-digit numbers, representing a low cognitive load. Level 2 involved adding two double-digit numbers, requiring additional mental computation and occasional carry operations, thereby increasing cognitive demand. Level 3 comprised adding two triple-digit numbers, which imposed the highest cognitive load due to the need for multiple carry operations and increased working-memory engagement[50,51]. This structured progression ensured a controlled and repeatable increase in cognitive load across experimental trials.

Throughout the experiment, PPG and IPG signals were continuously recorded for subsequent analysis. The experimental setup, illustrated in Fig. 2(b), was conducted in a quiet room with sufficient ambient lighting to minimize external disturbances. One laptop was dedicated to running the stimulation program, while a second laptop managed real-time acquisition of physiological signals. During each trial, participants' reaction times and error rates were recorded. Reaction time was defined as the interval between stimulus presentation and the participant's response, recorded when they entered the result in the input box. The accuracy of each response was automatically evaluated by the stimulation program.

Signal processing

Figure 3 illustrates the signal-processing and feature-extraction workflow for the fused feature set, comprising features from PPG, IPG, and their combination.

PPG signals

For PPG signal processing, the raw waveform is segmented using a sliding window and filtered with a digital band-pass filter (0.1–5 Hz) to isolate pulsatile components associated with cardiac activity. Within each segment, several time-domain features are extracted, including the maximum, minimum, mean, and standard deviation of the PPG waveform. Frequency-domain features are obtained via the discrete Fourier transform (DFT) and include the dominant frequency and its corresponding magnitude, the mean magnitude of all frequency components, and the total spectral power.

Furthermore, HRV-related metrics are derived to evaluate autonomic nervous system activity. A peak-detection algorithm[52] identifies systolic peaks, from which inter-beat intervals (IBIs) are computed. These IBIs are then used to calculate the standard deviation of normal-to-normal (NN) intervals (SDNNs), a widely recognized HRV index and marker of autonomic regulation[53,54]. The detected peaks are also utilized to compute PTT in conjunction with the IPG signal, enabling integrated cardiovascular assessment.

IPG signals

The IPG signals undergo a similar preprocessing pipeline, including segmentation and band-pass filtering to isolate pulsatile components. In addition to time-domain statistical features analogous to those extracted from the PPG signal, the feature set also incorporates morphological and temporal parameters, such as the systolic rise time (interval from the waveform foot to its peak) and systolic wave height (amplitude from baseline to peak). These morphological features capture dynamic variations in vascular impedance, offering valuable insights into blood-flow dynamics under cognitive load as well as arterial compliance and tissue elasticity[55,56].

PPG-IPG signal fusion

The combined feature derived from both PPG and IPG signals, PTT, is also computed. PTT integrates the temporal dynamics of the two modalities to capture complementary physiological information. It is calculated as the time delay between the systolic peak of the PPG waveform, which marks the onset of the pulse wave at the neck, and the systolic peak of the IPG waveform, representing the arrival of the pulse wave at the forehead. Because the arterial path to the neck is shorter, the pulse wave reaches this location earlier than the forehead, resulting in a measurable delay. This delay, defined as PTT, provides valuable insight into the characteristics of the intermediate arterial segment and serves as a non-invasive, indirect marker of arterial compliance, vascular responsiveness to cognitive load, and overall vascular health[57,58].

To ensure measurement accuracy, hardware and software-induced timing offsets are corrected through a calibration procedure. In this process, both sensors are temporarily placed at nearly the same location to identify and compensate for synchronization discrepancies.

By extracting features from the PPG, IPG, and their fusion, the system enables a comprehensive assessment of arterial dynamics that reflect both cardiac function and vascular responses to cognitive load[59–61]. This multimodal approach captures complementary information from central and peripheral pulse waveforms, enhancing the system's ability to characterize hemodynamic changes driven by autonomic regulation. TABLE I summarizes the mathematical formulas and corresponding descriptions used to compute the 29 features extracted from each segment of the PPG and IPG signals, as previously described.

Table 1. Multimodal feature set derived from PPG, IPG, and fused signals.

Feature	Description	Mathematical formula [a]
PPG_Max/IPG_Max	Maximum value of segmented PPG/IPG signals	$x_{\max}^{(m)} = \max_{0\le \ell < L}\, x[n_m+\ell]$
PPG_Min/IPG_Min	Minimum value of segmented PPG/IPG signals	$x_{\min}^{(m)} = \min_{0\le \ell < L}\, x[n_m+\ell]$
PPG_Mean/IPG_Mean	Mean value of segmented PPG/IPG signals	$\mu^{(m)} = \frac{1}{L}\sum_{\ell=0}^{L-1} x[n_m+\ell]$
PPG_STD/IPG_STD	Standard deviation of segmented PPG/IPG signals	$\sigma^{(m)} = \sqrt{\frac{1}{L}\sum_{\ell=0}^{L-1}\left(x[n_m+\ell]-\mu^{(m)}\right)^2}$
PPG_FFT_Dom_Freq/ IPG_FFT_Dom_Freq	Dominant frequency component of PPG/IPG signals	$X^{(m)}[k] = \sum_{\ell=0}^{L-1} x[n_m+\ell]\cdot e^{-j\frac{2\pi}{L}k\ell}$; $f_{\max}^{(m)} = \arg\max_k \left\lvert X^{(m)}[k]\right\rvert$
PPG_FFT_Dom_Mag/ IPG_FFT_Dom_Mag	Magnitude at the dominant frequency of PPG/IPG signals	$\lvert X\rvert_{\max}^{(m)} = \max_k \left\lvert X^{(m)}[k]\right\rvert$
PPG_FFT_Mean_Mag/ IPG_FFT_Mean_Mag	Mean magnitude of the frequency components of PPG/IPG signals	$\mu_{X[k]}^{(m)} = \frac{1}{L}\sum_{k=0}^{L-1}\left\lvert X^{(m)}[k]\right\rvert$
PPG_FFT_Total_Power/ IPG_FFT_Total_Power	Total spectral power of segmented PPG/IPG signals	$P_{X[k]}^{(m)} = \frac{1}{L}\sum_{k=0}^{L-1}\left\lvert X^{(m)}[k]\right\rvert^2$
HRV_IBI_Mean	Mean inter-beat interval	$\mu_{IBI}^{(m)} = \frac{1}{N_m}\sum_{i=1}^{N_m} IBI_i^{(m)}$
HRV_SDNN	Standard deviation of NN intervals (SDNN)	$\sigma_{IBI}^{(m)} = \sqrt{\frac{1}{N_m}\sum_{i=1}^{N_m}\left(IBI_i^{(m)}-\mu_{IBI}^{(m)}\right)^2}$
PTT_Max	Maximum of pulse transit time	$PTT_i^{(m)} = t_{IPG,foot}^{(m,i)} - t_{PPG,foot}^{(m,i)}$; $PTT_{\max}^{(m)} = \max_{1\le i<N_m} PTT_i^{(m)}$
PTT_Min	Minimum of pulse transit time	$PTT_{\min}^{(m)} = \min_{1\le i<N_m} PTT_i^{(m)}$
PTT_Mean	Mean of pulse transit time	$\mu_{PTT}^{(m)} = \frac{1}{N_m}\sum_{i=1}^{N_m} PTT_i^m$
PTT_Mean	Median of pulse transit time	$Med_{PTT}^{(m)} = \text{Median}\left\{PTT_i^{(m)}\right\}_{i=1}^{N_m}$
PTT_STD	Standard deviation of pulse transit time	$\sigma_{PTT}^{(m)} = \sqrt{\frac{1}{N_m}\sum_{i=1}^{N_m}\left(PTT_i^{(m)}-\mu_{PTT}^{(m)}\right)^2}$
SysHeight_Mean	Mean impedance systolic wave height	$\mu_{ISWH}^{(m)} = \frac{1}{N_m}\sum_{i=1}^{N_m} ISWH_i^{(m)}$
SysHeight_STD	Standard deviation of impedance systolic wave height	$\sigma_{ISWH}^{(m)} = \sqrt{\frac{1}{N_m}\sum_{i=1}^{N_m}\left(ISWH_i^{(m)}-\mu_{ISWH}^{(m)}\right)^2}$
SysHeight_Median	Median impedance systolic wave height	$Med_{ISWH}^{(m)} = \text{Median}\left\{ISWH_i^{(m)}\right\}_{i=1}^{N_m}$
RiseTime_Mean	Mean impedance rise time	$\mu_{IRT}^{(m)} = \frac{1}{N_m}\sum_{i=1}^{N_m} IRT_i^{(m)}$
RiseTime_STD	Standard deviation of impedance rise time	$\sigma_{IRT}^{(m)} = \sqrt{\frac{1}{N_m}\sum_{i=1}^{N_m}\left(IRT_i^{(m)}-\mu_{IRT}^{(m)}\right)^2}$
RiseTime_Median	Median impedance rise time	$Med_{IRT}^{(m)} = \text{Median}\left\{IRT_i^{(m)}\right\}_{i=1}^{N_m}$

[a] N_m: Heartbeat count per window; L: analysis window length (in samples); x: time-domain signal (in samples); X: DFT of x; $ISWH$ = impedance systolic wave height; IRT = impedance rise time; IBI = inter-beat interval; (m) window index m; n_m: start index of analysis window m.

Based on the extracted feature sets from PPG, IPG, and their fusion, a feature attribution algorithm is applied to determine which features contribute most significantly to the performance of the machine learning classification model. Among the commonly used methods, Gini importance, also known as mean decrease in impurity (MDI), is frequently adopted in tree-based models such as Decision Trees, Random Forests, and XGBoost. This technique quantifies feature importance by measuring the total reduction in node impurity, typically calculated using the Gini index, attributable to each feature across all decision splits in the model ensemble. The resulting importance scores are aggregated and ranked to reflect each feature's relative contribution to predictive accuracy[62].

Classification models

This study explores cognitive load classification using three widely adopted machine learning models: Decision Tree, Random Forest (RF), and Extreme Gradient Boosting (XGBoost). Two classification tasks are addressed: (1) a binary classification that distinguishes between the resting state and engagement in an arithmetic task, and (2) a multiclass classification that differentiates among the resting state and three distinct levels of arithmetic difficulty, referred to as Level 1, Level 2, and Level 3. These levels correspond to progressively increasing degrees of cognitive load, aligned with the difficulty levels of the arithmetic stimulation tasks.

Decision Tree is a machine learning model that organizes decision-making in a tree structure, allowing predictions to be made based on input features. Each internal node evaluates a condition on a specific feature, each branch represents the outcome of that condition, and each leaf node assigns a class label in classification tasks. The tree is built recursively by selecting features and thresholds that maximize class separation, typically evaluated using criteria such as Gini impurity or entropy. Growth continues until a predefined stopping condition is met, such as a maximum tree depth or a minimum number of samples per node. Decision Trees are widely used due to their interpretability, ability to handle both categorical and numerical data, and effectiveness in modeling complex decision boundaries[63].

RF is an ensemble learning method that extends Decision Tree algorithm by constructing a collection of trees instead of relying on a single one. Each tree is trained on a random subset of the training data and features, and predictions are aggregated using majority voting for classification tasks. This ensemble approach mitigates overfitting and generally improves predictive performance compared to individual decision trees[64].

XGBoost is a high-performance ensemble technique that addresses several limitations of RF. Unlike Random Forest, which trains trees independently, XGBoost builds trees sequentially, with each new tree aiming to correct the residual errors of the previous ensemble using a gradient boosting framework. This iterative learning strategy enables faster convergence, better management of the bias–variance trade-off, and often superior predictive accuracy in practical applications, as demonstrated in numerous studies[65].

These models learn to associate patterns in the extracted features with varying levels of cognitive load and perform final classification based on these learned representations.

The training process employed three evaluation strategies: subject-dependent, subject-independent, and mixed-subject. In the subject-dependent approach, the model was trained and tested on data from the same individual, resulting in 15 distinct machine-learning models, one corresponding to each participant, trained and validated independently. In the subject-independent approach, the emphasis was on assessing model generalizability across individuals. Data from 14 participants were combined to form the training set, while the data from the remaining participant served as the test set. This procedure followed a leave-one-subject-out cross-validation scheme, repeated 15 times to ensure that each participant's data was used once for testing. In the mixed-subject strategy, data from all participants were pooled and partitioned into five folds. Four folds were used for training and the remaining fold for testing, with the process repeated across all folds. The average testing accuracy across the five folds was then computed to evaluate performance.

Results and Discussion

PPG and IPG segmented data

Figure 4 presents a representative segment of the filtered PPG signal alongside the concurrently recorded IPG signal. It illustrates the computation of the IBI feature, defined as the time interval between two successive systolic peaks in the PPG waveform, which serves as a measure of beat-to-beat variability. For the IPG signal, the figure also demonstrates the extraction of morphological features, including systolic rise time and wave height, to characterize the vascular impedance response to pulse wave propagation. Both signals clearly capture the systolic and diastolic phases of the cardiac cycle, enabling robust extraction of pulse-related features. Additionally, the figure highlights the computation of PTT, defined as the temporal delay between the systolic peaks of the PPG and IPG waveforms, which reflects the travel time of the pulse wave between the two sensing sites.

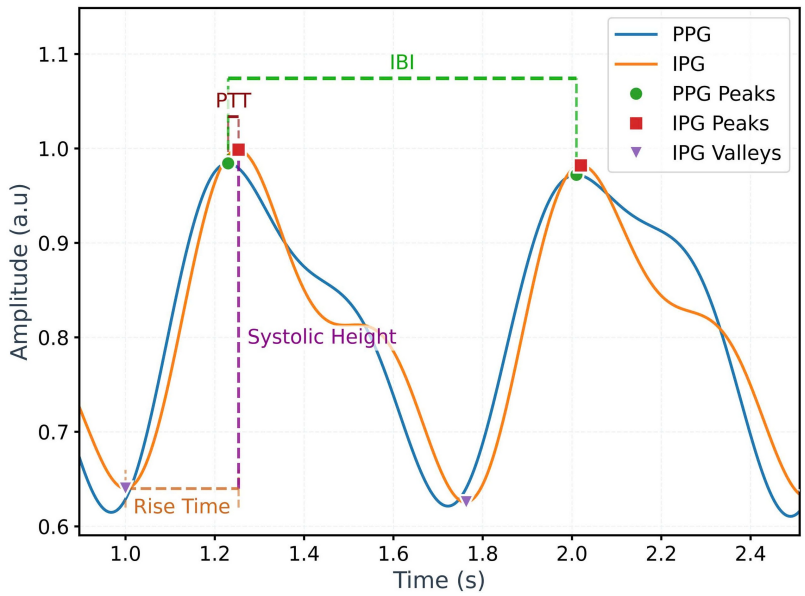

Figure 4. Representative PPG and IPG waveforms with extracted features highlighted.

Reaction time and error rate

Figure 5 illustrates the relationship between reaction time and error rate across the three levels of arithmetic task difficulty. A moderate to strong positive correlation is observed at all levels, indicating that participants who responded more slowly tended to make more errors. Notably, Level 2 exhibited the strongest correlation, with a Pearson coefficient of $r = 0.74$. Level 3, which represents the highest cognitive demand, is associated with both the longest reaction times (ranging from 4.6 to 8 seconds) and the highest error rates (reaching up to 60%), underscoring the increased task difficulty. Although Levels 1 and 3 show similar correlation coefficients (approximately 0.6), the wider spread of data points in Level 3 suggests greater variability in both response time and performance. This pattern reflects the heightened cognitive load and response inconsistency elicited by more complex tasks.

Feature visualization

Feature visualization with t-SNE

Figure 6 presents the two-dimensional projection of 29 features extracted from the PPG, IPG, and fused PPG–IPG datasets using the t-SNE algorithm, which transforms high-dimensional data into a lower-dimensional space for visualization[66]. The projection includes data from all mixed-subject trials, enabling an overall assessment of class separability across participants. In the binary classification scenario (Fig. 6(a)), the projected feature distribution reveals a distinct separation between the resting state and the arithmetic-induced cognitive load condition, indicating strong discriminative potential of the extracted features in distinguishing between low and high cognitive demand.

In contrast, the four-class scenario (Fig. 6(b)), which represents the resting state and three increasing levels of cognitive load, exhibits substantial overlap among clusters corresponding to different task difficulties. This reduced class separability reflects the challenge of differentiating between subtle gradations of cognitive load, particularly under mixed-subject conditions where inter-individual variability may further obscure class boundaries. These observations emphasize the complexity of multiclass cognitive load classification and suggest the need for more advanced feature representations or subject-specific modeling strategies to improve discrimination among intermediate workload levels.

Feature importance

Figure 7 presents the feature importance rankings obtained from the RF model. In both the binary (Fig. 7(a)) and four-class (Fig. 7(b)) classification tasks, IPG-derived features dominate. The four most informative features across both settings are the mean amplitude of the IPG segment, the maximum and minimum IPG values within the segment, and the average amplitude of the PPG segment. Among these, the mean IPG amplitude consistently ranks as the top contributor.

The higher importance of IPG-derived features can be explained by the fundamental physiological differences between IPG and PPG. We hypothesize that carotid PPG primarily reflects global cerebral perfusion, while frontal IPG captures localized hemodynamic responses related to task-specific neural activity. This aligns with the mechanism of neurovascular coupling

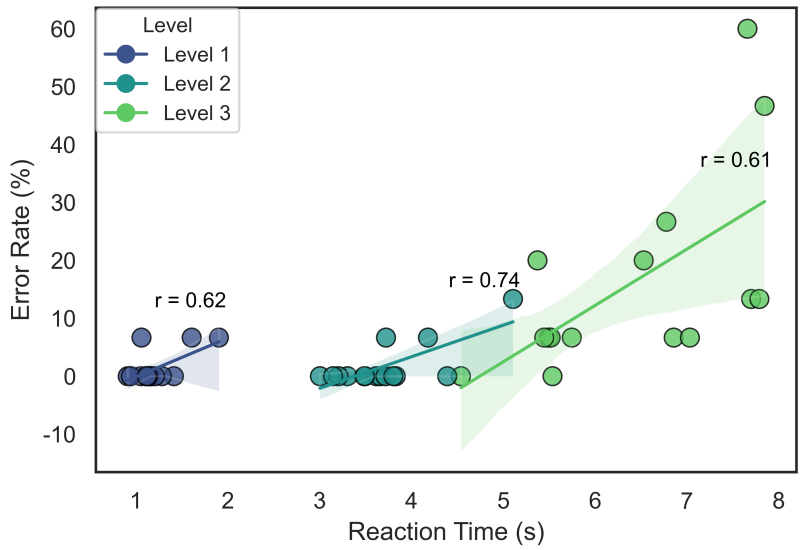

Figure 5. Relationship between reaction time and error rate across three levels of arithmetic task difficulty.

(NVC). Mental arithmetic tasks strongly activate the prefrontal cortex (PFC), increasing its metabolic demand[67,68]. NVC triggers local vasodilation in the PFC, leading to region-specific increases in cerebral blood flow and blood volume[56].

Because the IPG sensor was placed directly over the PFC, it is well positioned to detect these localized impedance changes. In contrast, carotid PPG reflects broader cerebral blood flow and is less sensitive to localized cortical activation. As a result, IPG-derived features provide a more direct and sensitive representation of load-related neural activity, explaining their higher importance in the classification model.

Furthermore, the top seven features remain consistent across the two scenarios, collectively accounting for the majority of the importance scores within the classification model. While their exact ranking order differs slightly between the binary and four-class cases, all seven features consistently appear among the most dominant, underscoring their robustness in cognitive load decoding. Notably, these top-ranked features are primarily time-domain statistical descriptors, highlighting their critical role as indicators of cognitive load. This suggests that temporal variations in signal magnitude, particularly from the IPG modality, are highly informative for distinguishing cognitive states.

Figure 8 illustrates the distribution of the top seven contributing features, averaged across all subjects and grouped into four cognitive states: Resting (Relax), Level 1, Level 2, and Level 3 of arithmetic-induced cognitive load. Prior to visualization, the features were independently normalized for the IPG and PPG modalities to ensure comparability. The radar plot reveals distinct distribution patterns between the resting and task-engaged states. In the resting condition, higher values are observed for IPG-related features, including IPG_Max, IPG_Min, IPG_Mean, and RiseTime_Median. In contrast, during arithmetic tasks, the distribution shifts toward PPG-derived features, specifically PPG_Mean, PPG_Min, and PPG_Max, and is accompanied by a reduction in the values of the IPG-related features. This shift indicates a transition in physiological signal dominance from impedance-based features to PPG-based features as cognitive load increases.

Across the three workload levels, the feature distributions retain similar shapes with substantial overlap, making Level 1, Level 2, and Level 3 difficult to distinguish based solely on these features. RiseTime_Median shows the largest variability but does not follow a consistent trend across conditions, suggesting limited reliability as an indicator of cognitive load intensity.

The observed patterns reflect the complementary effects of systemic autonomic regulation and localized neurovascular coupling during cognitive stress. Increased cognitive demand activates sympathetic cardiovascular control, elevating arterial pressure and central pulsatility to sustain cerebral perfusion, which accounts for the increased carotid PPG features[69–71]. Concurrently, enhanced prefrontal neural activity induces neurovascular coupling and functional hyperemia, increasing local blood volume[72,73]. Because blood is more conductive than surrounding tissue, this results in reduced forehead bioimpedance, explaining the decrease in IPG features. Thus, within this measurement setup, PPG primarily reflects systemic sympathetic arousal, whereas IPG captures localized hemodynamic recruitment associated with cortical activation.

Tracking both IPG and PPG therefore provides complementary insight into vascular reactivity and autonomic nervous system modulation.

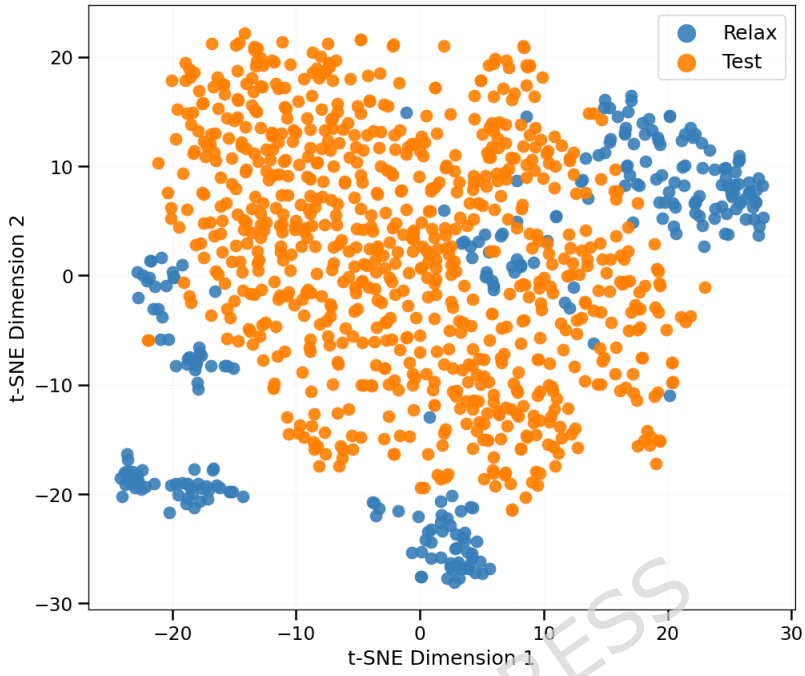

(a)

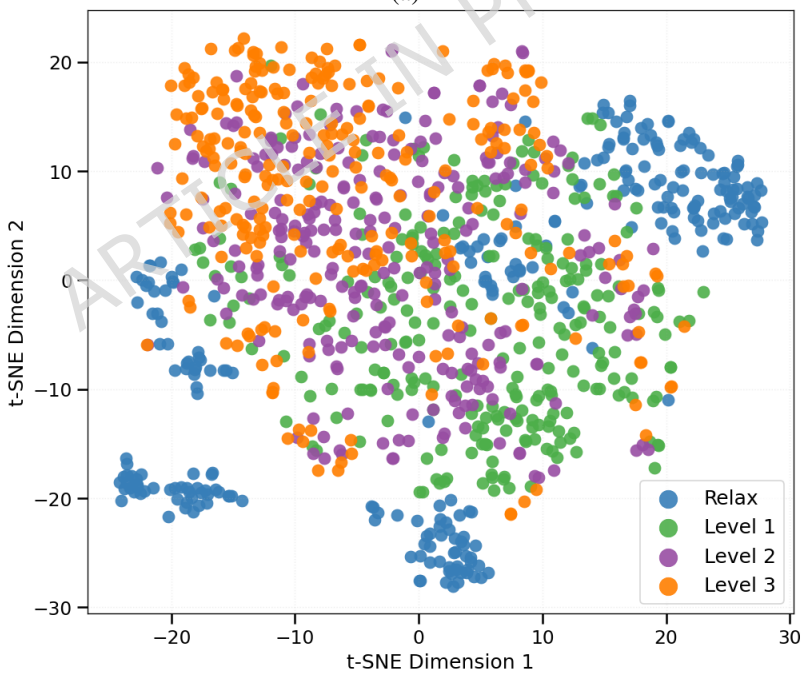

(b)

Figure 6. Feature visualization of the multidimensional fusion features extracted from PPG and IPG signals using the t-SNE algorithm for (a) the two class classification problem and (b) the four class classification problem in cognitive load categorization.

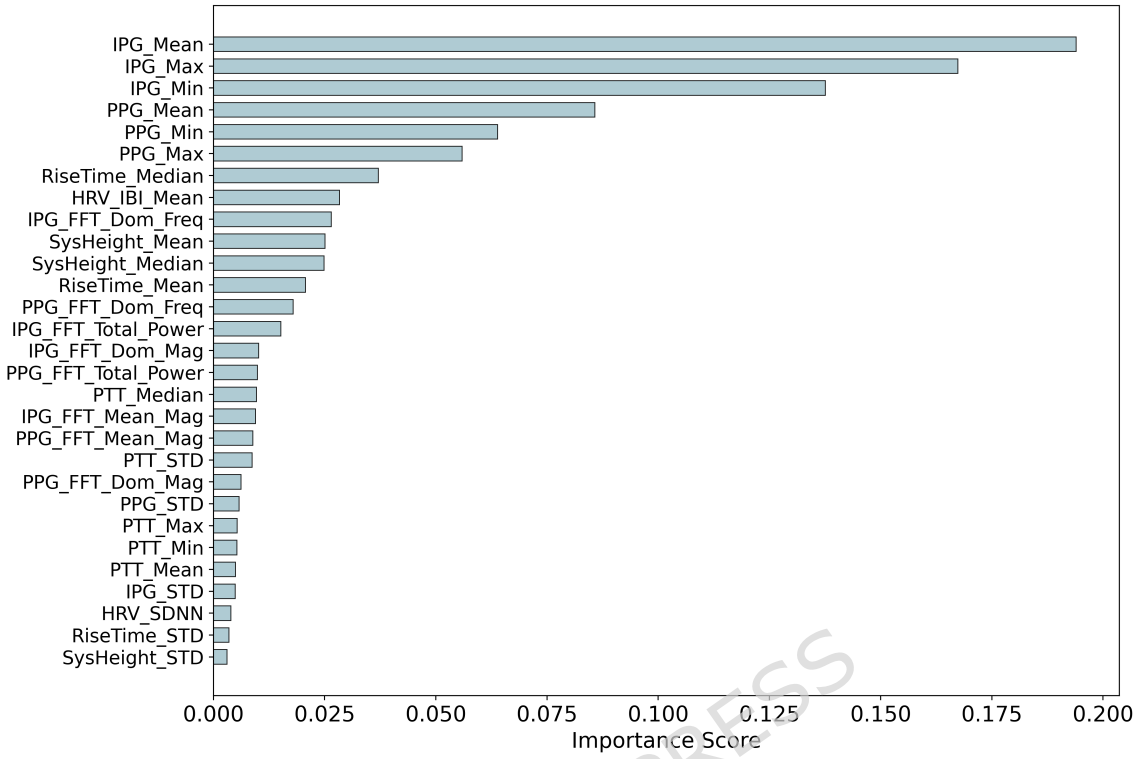

(a)

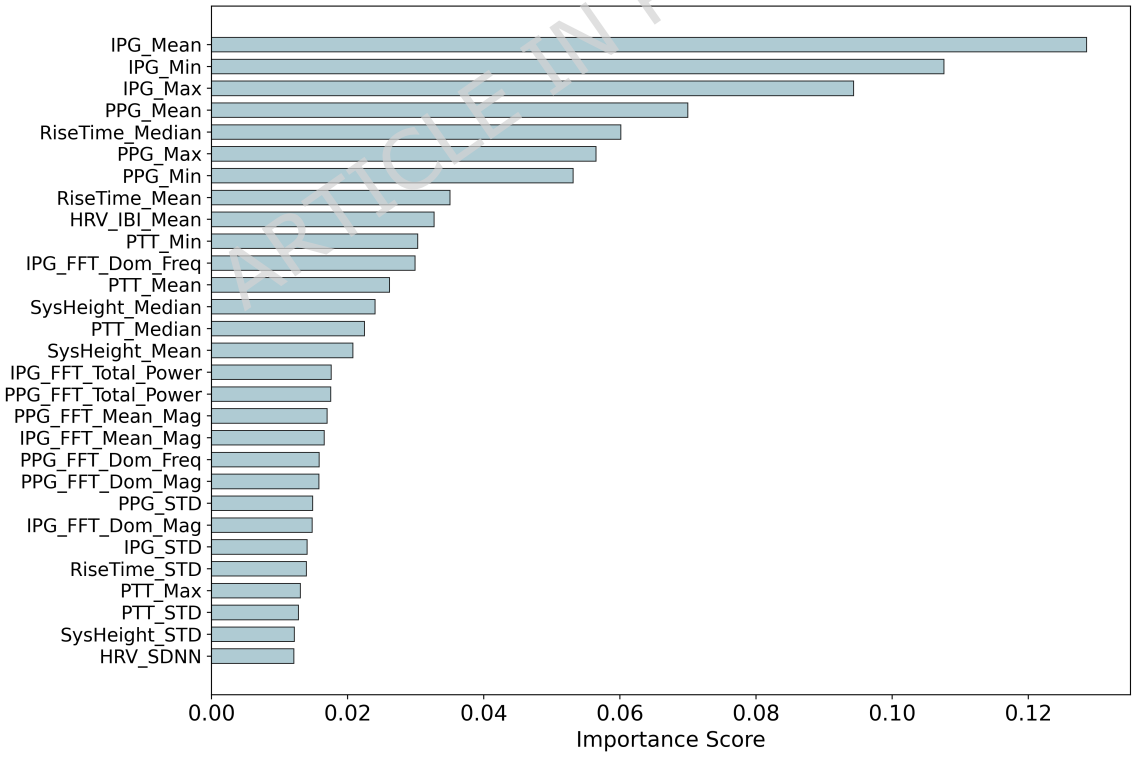

(b)

Figure 7. Feature-importance rankings for cognitive workload classification during arithmetic tasks: (a) two-class, and (b) four-class settings.

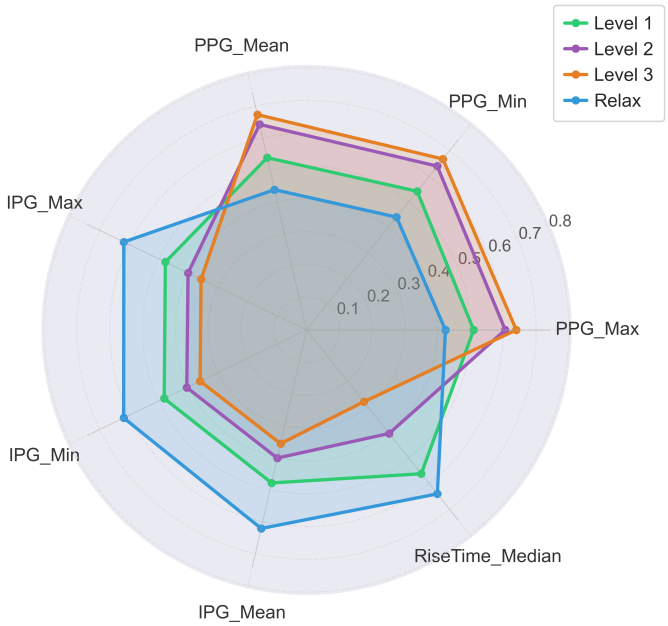

Figure 8. Distributions of the top four contributing feature values across four cognitive load classes.

Classification results

Figure 9 presents the average classification accuracies across all participants for two classification tasks: a 2-class problem that distinguishes between Relax and cognitive load, and a 4-class problem that includes Relax, Level 1, Level 2, and Level 3 cognitive states. The results compare the performance of three evaluation strategies, namely subject-independent, mix-subject, and subject-dependent, applied across three machine learning algorithms: Decision Tree, RF, and XGBoost.

Two-class cognitive task classification

In the 2-class classification task, shown in Fig. 9(a), all models achieved high average accuracy (> 95%) under both the mix-subject and subject-dependent strategies. These two approaches consistently outperformed the subject-independent setting, where all models yielded an accuracy around 90%. Notably, under the subject-dependent condition, all three models reached perfect classification accuracy of 100%. This finding suggests that when the model is trained and tested on data from the same individual, it can nearly achieve flawless discrimination between resting and workload states. In contrast, generalizing across subjects remains more challenging due to individual variability in physiological responses.

Four-class cognitive task classification

For the 4-class classification task (Fig. 9(b)), overall accuracies decreased across all models, reflecting the greater difficulty of distinguishing multiple workload levels. In the subject-dependent setting, RF achieved the highest accuracy (96%), demonstrating its effectiveness in capturing intra-subject physiological patterns. In contrast, subject-independent performance dropped notably, with RF reaching 66%, XGBoost 65%, and Decision Tree 60%. For the mix-subject evaluation, XGBoost (87%) and RF (83%) performed substantially better than Decision Tree (65%).

The sharp decline from subject-dependent accuracy (up to 100%) to subject-independent accuracy (as low as 60%) is a key finding. This gap is primarily due to strong inter-individual variability in baseline cardiovascular metrics, skin impedance, and autonomic responses to mental load. Additionally, small differences in sensor placement and morphology across subjects can affect waveform characteristics. These factors hinder the generalization ability of subject-independent models and suggest that practical implementations will likely require a brief user-specific calibration phase to ensure reliable performance.

Comparison between binary and four-class tasks

Overall, these results demonstrate that subject-dependent classification yields the highest accuracy, as it benefits from consistent physiological patterns within individuals. In contrast, subject-independent models are hindered by inter-individual variability in baseline physiology and cognitive load responses. Furthermore, the performance gap between the 2-class and 4-class problems highlights the challenge of detecting subtle differences in cognitive load. Among the three models, RF delivered the best performance in 4 out of 6 scenarios, closely followed by XGBoost, which achieved 3 out of 6 top scores. Both models reached 100% accuracy in the 2-class subject-dependent case, confirming their strong capacity for personalized cognitive state classification.

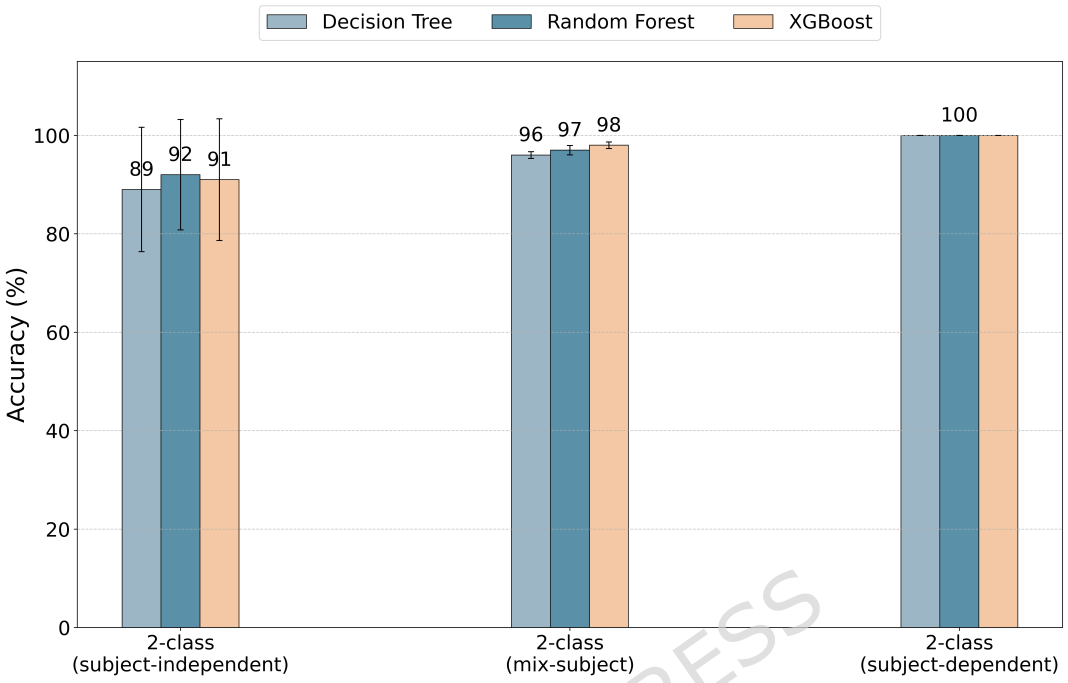

(a)

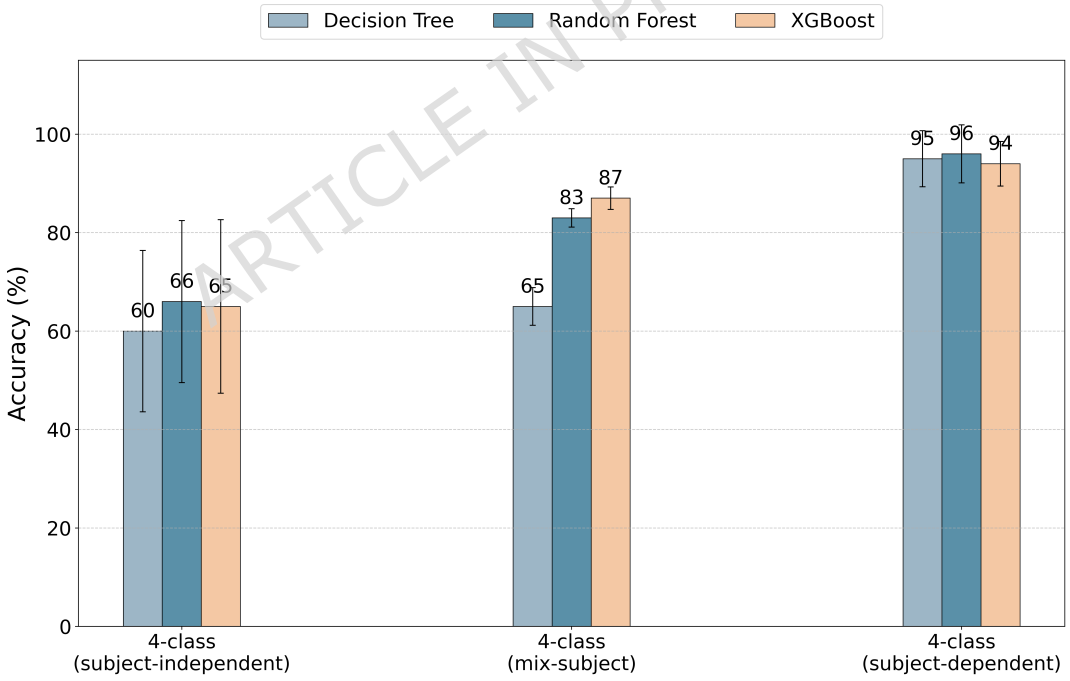

(b)

Figure 9. Classification performance for cognitive load was evaluated in (a) a two class scenario (Relax vs. Task) and (b) a four class scenario (Relax, Level 1, Level 2, Level 3), using both subject dependent and subject independent approaches, and compared across three machine learning algorithms.

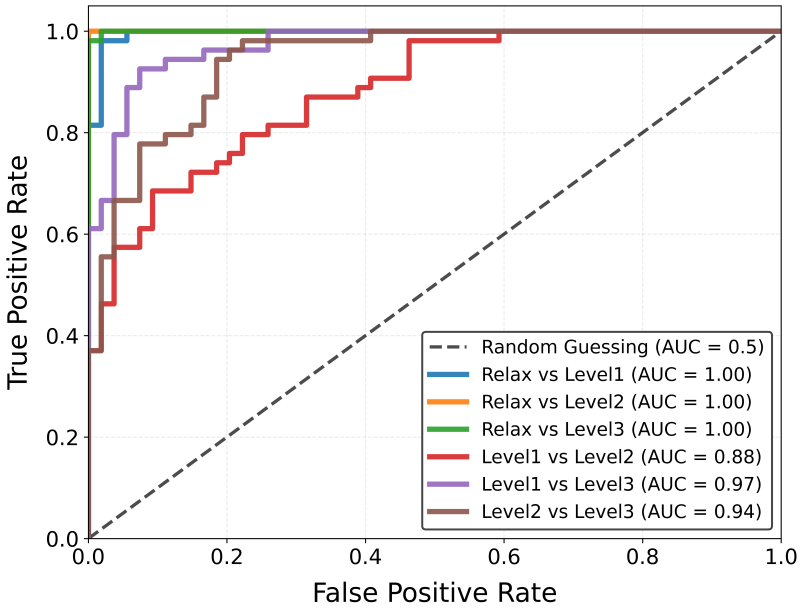

Figure 10. ROC analysis for the four-class cognitive classification problem based on Random Forest algorithm, using the mixed-subject strategy.

To further evaluate multiclass classification performance, Fig. 10 presents the receiver operating characteristic (ROC) curves for one-versus-one binary classifications among the four cognitive states using the RF algorithm under the mixed-subject strategy. These curves illustrate the model's ability to distinguish between each pair of cognitive load levels. The highest performance, with an area under the curve (AUC) of 1.0, was achieved when classifying the Relax condition against Level 1, Level 2, or Level 3. This reflects a clear distinction between the resting state and any level of cognitive load.

In contrast, lower AUC values were observed for comparisons among the three workload levels, underscoring the increased difficulty in distinguishing between varying degrees of mental effort. Despite this challenge, the model demonstrated strong performance in separating Level 1 from Level 3 (AUC = 0.97) and Level 2 from Level 3 (AUC = 0.94). However, its ability to differentiate between Level 1 and Level 2 declined, yielding a lower AUC of 0.88. This pattern suggests that cognitive workload may vary along a continuum rather than forming sharply distinct categories. Moreover, starting from a minimal cognitive state during rest, mental effort may increase gradually with the onset of low-difficulty tasks and then accelerate more rapidly as task complexity continues to rise[74–76]. Future research should consider modeling cognitive load as a continuous variable. Approaching the problem through regression may allow for more fine-grained and accurate decoding of cognitive effort.

Incorporating ECG in future studies could offer deeper insights into cardiovascular dynamics and complement the information provided by PPG and IPG measurements. As cognitive load originates in the brain and induces systemic physiological responses through the autonomic nervous system, ECG is well-suited to capture subtle or delayed cardiac changes associated with cognitive stress. By integrating ECG with PPG and IPG, the system could provide a more comprehensive view of brain–heart interactions and the body's adaptive mechanisms in response to varying mental demands[23,77].

A limitation of this study lies in the experimental protocol, in which arithmetic tasks were presented sequentially with increasing difficulty and separated by a brief 15-s rest period, potentially allowing cognitive fatigue to accumulate. Consequently, physiological responses at higher levels may reflect both task difficulty and fatigue effects. While this does not undermine the study's primary objective of classifying progressively increasing cognitive load states, future work will employ randomized or counterbalanced task orders and statistical control of trial order or time-on-task effects to better disentangle these factors[78]. In addition, studies with larger and more diverse cohorts, along with baseline measures of cognitive ability and arithmetic proficiency, are planned to improve statistical power and account for inter-individual variability.

From a hardware perspective, the current neck placement of the PPG sensor may cause discomfort during prolonged use. Future designs will prioritize printed circuit board miniaturization, the use of flexible materials, and wireless communication to improve wearability, mobility, and user comfort.

In addition, future work will explore deep learning approaches, including convolutional neural networks, recurrent neural networks, and attention-based multimodal fusion models, to enable end-to-end learning directly from raw PPG and IPG signals. With larger datasets, these approaches are expected to further improve classification accuracy, robustness across subjects, and multimodal integration.

Conclusions

This study presents a synergistic framework that integrates global, localized, and fused cardiovascular measurements to characterize cerebral hemodynamics under cognitive load. Specifically, carotid PPG was used to assess global cerebral perfusion, frontal IPG captured localized blood volume changes in the engaged cortical region, and pulse transit time between the neck and forehead reflected arterial properties along the intervening pathway. The experimental results show that features extracted from both signals enable accurate classification of cognitive load levels, highlighting strong brain–heart interactions governed by neurovascular and autonomic mechanisms[20,79,80]. Notably, heart rate variability and IPG-based indices were particularly sensitive to task difficulty, with IPG-derived features contributing most strongly to workload discrimination, underscoring the value of region-specific monitoring for cognitive state assessment.

Among the evaluated features, IPG-derived metrics that reflect localized neurovascular coupling within the prefrontal cortex consistently dominated the classification models. This key finding indicates that regional hemodynamic responses provide more informative markers of cognitive load than global perfusion measures or the fused PTT feature, underscoring the novelty and physiological relevance of the proposed approach. These results further highlight the substantial metabolic demands associated with cognitive processing and the importance of dynamic regulation of cerebral blood flow. Taken together, global perfusion assessed via PPG and localized cerebral blood volume changes captured through IPG provide complementary and physiologically meaningful insights into cognitive engagement.

While our primary goal was to explore a non-EEG alternative, it is useful to contextualize our results relative to existing EEG-based workload detection studies. In subject-dependent evaluations, many EEG systems report accuracies in the 80–95% range for binary or multi-level mental arithmetic tasks, with some deep-learning models achieving approximately 94–97% under optimized conditions. The proposed framework achieved a subject-dependent accuracy of 96% for the four-class task, placing it within the upper range of EEG-based performance. Although the subject-independent accuracy (around 65%) is lower, this trend is consistent with the EEG literature, where cross-subject generalization typically drops substantially without subject-specific calibration[81–84].

In conclusion, the proposed multimodal PPG–IPG framework demonstrates strong potential for accurate multi-level cognitive load classification and offers promising applications in adaptive human–machine interaction and real-world monitoring. Continuous workload estimation could enable adaptive systems to regulate information flow, adjust task difficulty, or suppress non-critical alerts in high-demand environments such as aviation, driving, and industrial operations, thereby reducing cognitive overload and enhancing safety. In educational and training contexts, real-time workload feedback may support personalized learning by dynamically adapting task difficulty or identifying periods of excessive mental strain. Moreover, in operational settings including healthcare, transportation, and security monitoring, wearable PPG–IPG systems could facilitate early detection of cognitive fatigue, enabling timely intervention and improved performance.

References

1. DiDomenico, A. & Nussbaum, M. A. Interactive effects of physical and mental workload on subjective workload assessment. *Int. journal industrial ergonomics* **38**, 977–983 (2008).
2. Tao, D. *et al.* A systematic review of physiological measures of mental workload. *Int. journal environmental research public health* **16**, 2716 (2019).
3. Luzzani, G., Buraioli, I., Demarchi, D. & Guglieri, G. A review of physiological measures for mental workload assessment in aviation: A state-of-the-art review of mental workload physiological assessment methods in human-machine interaction analysis. *The Aeronaut. J.* **128**, 928–949 (2024).
4. Pereira, E. *et al.* Capturing mental workload through physiological sensors in human–robot collaboration: A systematic literature review. *Appl. Sci.* **15**, 3317 (2025).
5. MacDonald, W. The impact of job demands and workload on stress and fatigue. *Aust. psychologist* **38**, 102–117 (2003).
6. Coughlin, J. F., Reimer, B. & Mehler, B. Monitoring, managing, and motivating driver safety and well-being. *IEEE Pervasive Comput.* **10**, 14–21 (2011).
7. Holden, R. J. *et al.* Effects of mental demands during dispensing on perceived medication safety and employee well-being: a study of workload in pediatric hospital pharmacies. *Res. social administrative Pharm.* **6**, 293–306 (2010).
8. Mirzabeigi, H., Anoosheh, V. S., Rostami, M. & Jalali, M. Subjective mental workload profile and human error probability in nurses: A cross-sectional analytical study. *Int. J. Environ. Heal. Eng.* **14**, 23 (2025).
9. Biondi, F. N., Cacanindin, A., Douglas, C. & Cort, J. Overloaded and at work: investigating the effect of cognitive workload on assembly task performance. *Hum. factors* **63**, 813–820 (2021).

10. Zhang, P., Wang, X., Zhang, W. & Chen, J. Learning spatial–spectral–temporal eeg features with recurrent 3d convolutional neural networks for cross-task mental workload assessment. *IEEE Transactions on neural systems rehabilitation engineering* **27**, 31–42 (2018).

11. Rosanne, O. *et al.* Adaptive filtering for improved eeg-based mental workload assessment of ambulant users. *Front. neuroscience* **15**, 611962 (2021).

12. Hogervorst, M. A., Brouwer, A. M. & Van Erp, J. B. Combining and comparing eeg, peripheral physiology and eye-related measures for the assessment of mental workload. *Front. neuroscience* **8**, 322 (2014).

13. Roy, R. N., Charbonnier, S., Campagne, A. & Bonnet, S. Efficient mental workload estimation using task-independent eeg features. *J. neural engineering* **13**, 026019 (2016).

14. Di Flumeri, G. *et al.* A neuroergonomic approach fostered by wearable eeg for the multimodal assessment of drivers trainees. *Sensors* **23**, 8389 (2023).

15. Dimitrakopoulos, G. N. *et al.* Task-independent mental workload classification based upon common multiband eeg cortical connectivity. *IEEE Transactions on Neural Syst. Rehabil. Eng.* **25**, 1940–1949 (2017).

16. Qu, H., Gao, X. & Pang, L. Classification of mental workload based on multiple features of ecg signals. *Informatics Medicine Unlocked* **24**, 100575 (2021).

17. Al Fawwaz, A., Rahma, O. N., Ain, K., Ittaqillah, S. I. & Chai, R. Measurement of mental workload using heart rate variability and electrodermal activity. *IEEE Access* **12**, 197589–197601 (2024).

18. Ginty, A. T., Kraynak, T. E., Fisher, J. P. & Gianaros, P. J. Cardiovascular and autonomic reactivity to psychological stress: Neurophysiological substrates and links to cardiovascular disease. *Auton. Neurosci.* **207**, 2–9 (2017).

19. Forte, G. & Casagrande, M. The intricate brain–heart connection: The relationship between heart rate variability and cognitive functioning. *Neuroscience* **565**, 369–376 (2025).

20. Valenza, G., Matić, Z. & Catrambone, V. The brain–heart axis: Integrative cooperation of neural, mechanical and biochemical pathways. *Nat. Rev. Cardiol.* 1–14 (2025).

21. Silvani, A., Calandra-Buonaura, G., Dampney, R. A. & Cortelli, P. Brain–heart interactions: physiology and clinical implications. *Philos. transactions royal society A: Math. physical engineering sciences* **374**, 20150181 (2016).

22. Blons, E. *et al.* Alterations in heart-brain interactions under mild stress during a cognitive task are reflected in entropy of heart rate dynamics. *Sci. reports* **9**, 18190 (2019).

23. Alshanskaia, E. I., Zhozhikashvili, N. A., Polikanova, I. S. & Martynova, O. V. Heart rate response to cognitive load as a marker of depression and increased anxiety. *Front. Psychiatry* **15**, 1355846 (2024).

24. Solhjoo, S. *et al.* Heart rate and heart rate variability correlate with clinical reasoning performance and self-reported measures of cognitive load. *Sci. reports* **9**, 14668 (2019).

25. Wagner, D. R. *et al.* Relationship between pulse transit time and blood pressure is impaired in patients with chronic heart failure. *Clin. research cardiology* **99**, 657–664 (2010).

26. Sara, J. D. S. *et al.* Mental stress and its effects on vascular health. *Mayo clinic proceedings* **97**, 951–990 (2022).

27. Dolmans, T. C., Poel, M., van't Klooster, J. W. J. & Veldkamp, B. P. Perceived mental workload classification using intermediate fusion multimodal deep learning. *Front. human neuroscience* **14**, 609096 (2021).

28. Ding, Y., Cao, Y., Duffy, V. G., Wang, Y. & Zhang, X. Measurement and identification of mental workload during simulated computer tasks with multimodal methods and machine learning. *Ergonomics* **63**, 896–908 (2020).

29. Zhou, T. *et al.* Multimodal physiological signals for workload prediction in robot-assisted surgery. *ACM Transactions on Human-Robot Interact. (THRI)* **9**, 1–26 (2020).

30. Park, J., Seok, H. S., Kim, S. S. & Shin, H. Photoplethysmogram analysis and applications: an integrative review. *Front. physiology* **12**, 808451 (2022).

31. Jacques, S. L. Optical properties of biological tissues: a review. *Phys. Medicine & Biol.* **58**, R37 (2013).

32. Reisner, A. *et al.* Utility of the photoplethysmogram in circulatory monitoring. *Anesthesiology* **108**, 950–958 (2008).

33. Ding, X. *et al.* Pulse transit time based continuous cuffless blood pressure estimation: A new extension and a comprehensive evaluation. *Sci. reports* **7**, 11554 (2017).

34. Abasi, S., Aggas, J. R., Garayar-Leyva, G. G., Walther, B. K. & Guiseppi-Elie, A. Bioelectrical impedance spectroscopy for monitoring mammalian cells and tissues under different frequency domains: A review. *ACS measurement science au* **2**, 495–516 (2022).

35. Jung, M. H. *et al.* Wrist-wearable bioelectrical impedance analyzer with miniature electrodes for daily obesity management. *Sci. reports* **11**, 1238 (2021).

36. Analog Devices. *AD5933: 1 MSPS, 12-Bit Impedance Converter, Network Analyzer* (2011). Datasheet.

37. Khalil, S. F., Mohktar, M. S. & Ibrahim, F. The theory and fundamentals of bioimpedance analysis in clinical status monitoring and diagnosis of diseases. *Sensors* **14**, 10895–10928 (2014).

38. Cornish, B. H., Thomas, B. J. & Ward, L. C. Improved prediction of extracellular and total body water using impedance loci generated by multiple frequency bioelectrical impedance analysis. *Phys. Medicine Biol.* **38**, 337 (1993).

39. Campa, F. *et al.* High-standard predictive equations for estimating body composition using bioelectrical impedance analysis: a systematic review. *J. Transl. Medicine* **22**, 515 (2024).

40. Wang, T. W. *et al.* Bio-impedance measurement optimization for high-resolution carotid pulse sensing. *Sensors* **21**, 1600 (2021).

41. De Lorenzo, A., Andreoli, A., Matthie, J. & Withers, P. Predicting body cell mass with bioimpedance by using theoretical methods: a technological review. *J. applied physiology* **82**, 1542–1558 (1997).

42. Ferreira, J., Pau, I., Lindecrantz, K. & Seoane, F. A handheld and textile-enabled bioimpedance system for ubiquitous body composition analysis. an initial functional validation. *IEEE journal biomedical health informatics* **21**, 1224–1232 (2016).

43. Kassanos, P., Constantinou, L., Triantis, I. F. & Demosthenous, A. An integrated analog readout for multi-frequency bioimpedance measurements. *IEEE Sensors J.* **14**, 2792–2800 (2014).

44. Creegan, A. *et al.* A wearable open-source electrical impedance tomography device. *HardwareX* **18**, e00521 (2024).

45. Sheingold, D. H. Impedance & admittance transformations using operational amplifiers. *Light. Empiricist* **12**, 1–8 (1964).

46. Berends, I. E. & Van Lieshout, E. C. The effect of illustrations in arithmetic problem-solving: Effects of increased cognitive load. *Learn. Instr.* **19**, 345–353 (2009).

47. Eesee, A. K., Varga, V., Eigner, G. & Ruppert, T. Impact of work instruction difficulty on cognitive load and operational efficiency. *Sci. Reports* **15**, 11028 (2025).

48. Gupta, U. & Zheng, R. Z. Cognitive load in solving mathematics problems: Validating the role of motivation and the interaction among prior knowledge, worked examples, and task difficulty. *Eur. J. STEM Educ.* **5**, 5 (2020).

49. Wang, J., Stevens, C., Bennett, W. & Yu, D. Granular estimation of user cognitive workload using multi-modal physiological sensors. *Front. Neuroergonomics* **5**, 1292627 (2024).

50. Spüler, M. *et al.* Eeg-based prediction of cognitive workload induced by arithmetic: a step towards online adaptation in numerical learning. *Zdm* **48**, 267–278 (2016).

51. Ding, Y. *et al.* Effects of working memory, strategy use, and single-step mental addition on multi-step mental addition in chinese elementary students. *Front. psychology* **10**, 148 (2019).

52. Makowski, D. *et al.* Neurokit2: A python toolbox for neurophysiological signal processing. *Behav. research methods* **53**, 1689–1696 (2021).

53. Gullett, N., Zajkowska, Z., Walsh, A., Harper, R. & Mondelli, V. Heart rate variability (hrv) as a way to understand associations between the autonomic nervous system (ans) and affective states: A critical review of the literature. *Int. J. Psychophysiol.* **192**, 35–42 (2023).

54. Grégoire, J. M., Gilon, C., Carlier, S. & Bersini, H. Heart rate variability (hrv) as a way to understand associations between the autonomic nervous system (ans) and affective states: A critical review of the literature. *Acta cardiologica* **78**, 648–662 (2023).

55. Karpiel, I., Richter-Laskowska, M., Feige, D., Gacek, A. & Sobotnicki, A. An effective method of detecting characteristic points of impedance cardiogram verified in the clinical pilot study. *Sensors* **22**, 9872 (2022).

56. Bai, Y., Ke, L., Du, Q., Tian, B. & He, Y. Study of blood supply to functional brain areas under memory load based on bioimpedance technology. *Biomed. Signal Process. Control.* **88**, 105550 (2024).

57. Hahn, J. O., Reisner, A. T. & Asada, H. H. Estimation of pulse transit time using two diametric blood pressure waveform measurements. *Med. engineering physics* **32**, 753–759 (2010).

58. Chen, Y. S., Lu, W. A., Hsu, L. Y. & Kuo, C. D. Determinants of hand pulse wave velocity and hand pulse transit time in healthy adults. *Sci. Reports* **14**, 10144 (2024).

59. McDuff, D. *et al.* Non-contact imaging of peripheral hemodynamics during cognitive and psychological stressors. *Sci. Reports* **10**, 10884 (2020).

60. Zhang, X. *et al.* Photoplethysmogram-based cognitive load assessment using multi-feature fusion model. *ACM Transactions on Appl. Percept. (TAP)* **16**, 1–17 (2019).

61. Debie, E. *et al.* Multimodal fusion for objective assessment of cognitive workload: A review. *Biomed. Signal Process. Control.* **51**, 1542–1555 (2019).

62. Nembrini, S., König, I. R. & Wright, M. N. The revival of the gini importance? *Bioinformatics* **34**, 3711–3718 (2018).

63. Charbuty, B. & Abdulazeez, A. Classification based on decision tree algorithm for machine learning. *J. applied science technology trends* **2**, 20–28 (2021).

64. Breiman, L. Random forests. *Mach. learning* **45**, 5–32 (2001).

65. Chen, T. & Guestrin, C. Xgboost: A scalable tree boosting system. *In Proc. 22nd acm sigkdd international conference on knowledge discovery data mining* 785–794 (2016).

66. Maaten, L. V. D. & Hinton, G. Visualizing data using t-sne. *J. machine learning research* **9**, 2579–2605 (2008).

67. Smith, E. E. & Jonides, J. Working memory: A view from neuroimaging. *Cogn. psychology* **33**, 5–42 (1997).

68. Phelps, E. A. Emotion and cognition: insights from studies of the human amygdala. *Annu. Rev. Psychol.* **57**, 27–53 (2006).

69. Pavlov, Y. G. *et al.* Task-evoked pulse wave amplitude tracks cognitive load. *Sci. Reports* **13**, 22592 (2023).

70. Heffernan, K. S. *et al.* Carotid artery stiffness and hemodynamic pulsatility during cognitive engagement in healthy adults: a pilot investigation. *Am. journal hypertension* **28**, 615–622 (2015).

71. Heffernan, K. S. *et al.* Arterial stiffness and cerebral hemodynamic pulsatility during cognitive engagement in younger and older adults. *Exp. Gerontol.* **101**, 54–62 (2018).

72. Yang, L., Zhao, W., Kan, Y., Ren, C. & Ji, X. From mechanisms to medicine: neurovascular coupling in the diagnosis and treatment of cerebrovascular disorders: a narrative review. *Indoor Air* **14**, 16 (2024).

73. Racz, F. S., Mukli, P., Nagy, Z. & Eke, A. Increased prefrontal cortex connectivity during cognitive challenge assessed by fnirs imaging. *Biomed. optics express* **8**, 3842–3855 (2017).

74. Gendolla, G. H. The intensity of mental effort:"the heart does not lie". *Synthese* **205**, 231 (2025).

75. Ekin, M., Krejtz, K., Duarte, C., Duchowski, A. T. & Krejtz, I. Prediction of intrinsic and extraneous cognitive load with oculometric and biometric indicators. *Sci. Reports* **15**, 5213 (2025).

76. Arutyunova, K. R. *et al.* Heart rate dynamics for cognitive load estimation in a driving simulation task. *Sci. Reports* **14**, 31656 (2024).

77. Tsai, Y. Y. *et al.* Photoplethysmography-based hrv analysis and machine learning for real-time stress quantification in mental health applications. *APL bioengineering* **9** (2025).

78. Zhu, H. *et al.* Mental fatigue under the thermoneutral environment in buildings: Effects of the constant and altered workload sequences. *Indoor Air* **2024**, 2210991 (2024).

79. Catrambone, V., Candia-Rivera, D. & Valenza, G. Intracortical brain-heart interplay: An eeg model source study of sympathovagal changes. *Hum. Brain Mapp.* **45**, e26677 (2024).

80. Wang, S., Wang, X., Zhao, Y., Xie, L. & Zhang, J. A feedback loop study of brain-heart interaction based on hep and hrv. *Biocybern. Biomed. Eng.* **45**, 181–188 (2025).

81. Safari, M., Shalbaf, R., Bagherzadeh, S. & Shalbaf, A. Classification of mental workload using brain connectivity and machine learning on electroencephalogram data. *Sci. Reports* **14**, 9153 (2024).

82. Korkmaz, O. E., Korkmaz, S. G. & Aydemir, O. Detection of multitask mental workload using gamma band power features. *Neural Comput. Appl.* **36**, 10915–10926 (2024).

83. Maghsoudi, A. & Shalbaf, A. Mental arithmetic task recognition using effective connectivity and hierarchical feature selection from eeg signals. *Basic Clin. Neurosci.* **12**, 817 (2021).

84. Kakkos, I. *et al.* Eeg fingerprints of task-independent mental workload discrimination. *IEEE J. Biomed. Heal. Informatics* **25**, 3824–3833 (2021).

Funding

This research is funded by Vietnam National University HoChiMinh City (VNU-HCM) under grant number: B2023-20-15.

Author contributions statement

D.N.H., T.N.T., K.T.T., and N.K.L. conceived the experiments, D.N.H., T.N.T., K.T.T., and N.K.L. conducted the experiments, D.N.H. and T.N.T. analysed the results, C.D.L., H.X.M., Q.L.H., and T.H.N. wrote the manuscript. All authors reviewed the manuscript.

Consent for Publication

All participants provided informed consent for the collection and publication of their identifying information and images in this online open-access publication.

Data Availability

Data used and analyzed in this study can be obtained from the corresponding author upon reasonable request.

Additional information

Competing interests The authors declare no competing interests.